DOI: 10.1002/chem.200700756

Synchrotron X-Ray Charge-Density Study of Coordination Polymer $[Mn(HCOO)_2(H_2O)_2]_\infty$

Rasmus D. Poulsen,[a] Mads R. V. Jørgensen,[a] Jacob Overgaard,[a] Finn K. Larsen,[a] Wolfgang Morgenroth,[a] Timothy Graber,[b] Yu-Sheng Chen,[b] and Bo B. Iversen*[a]

Abstract: Three high-quality single-crystal X-ray diffraction data sets have been measured under very different conditions on a structurally simple, but magnetically complex, coordination polymer, $[Mn(HCOO)_2(H_2O)_2]_\infty$ (**1**). The first data set is a conventional 100(2) K $Mo_{K\alpha}$ data set, the second is a very high resolution 100(2) K data set measured on a second-generation synchrotron source, while the third data set was measured with a tiny crystal on a high brilliance third-generation synchrotron source at 16(2) K. Furthermore, the magnetic susceptibility (χ) and the heat capacity (C_p) have been measured from 2 to 300 K on pressed powder. The charge density of **1** was determined from multipole modeling of the experimental structure factors, and overall there is good agreement between the densities obtained separately from the three data sets. When considering the fine density features, the two 100 K data sets agree well with each other, but show small differences to the 16 K data set. Comparison with ab initio theory suggests that the 16 K APS data set provides the most accurate density. Topological analysis of the metal–ligand bonding, experimental 3d orbital populations on the Mn atoms, and Bader atomic charges indicate quite ionic, high-spin metal atoms. This picture is supported by the effective moment estimated from the magnetization measurements (5.840(2) μ_B), but it is at variance with earlier spin density measurements from polarized neutron diffraction. The magnetic ordering originates from superexchange involving covalent interactions with the ligands, and non-ionic effects are observed in the static deformation density maps as well as in plots of the valence shell charge concentrations. Overall, the present study provides a benchmark charge density that can be used in comparison with future metal formate dihydrate charge densities.

Keywords: charge-density distribution · coordination polymers · magnetic properties · topological analysis · X-ray diffraction

Introduction

Coordination polymers (CP) provide a very attractive route for crystal engineering of functional materials.[1] Unlike porous zeolite frameworks, the structural identities of the reactants are preserved in the crystal, and the molecular assembly of CPs is reminiscent of building with Lego blocks. In the past decade hundreds of studies have explored the awesome structural diversity of CPs, and a wide range of interesting physical and chemical properties have been identified. Of particular interest are their gas sorption properties,[2] but many efforts have also focused on understanding their complex catalytic and magnetic properties.[3]

The present study concerns one of the simplest CPs, $[Mn(HCOO)_2(H_2O)_2]_\infty$ (**1**), and indeed this hydrated metal formate framework was first examined more than 40 years ago.[4] The compound, Figure 1, is composed of Mn ions linked by formate groups and water molecules. There are two distinct metal sites in the structure. In the first site, the Mn1 ions are octahedrally coordinated to six formate oxygen atoms creating layers in the *bc* plane. The ions in these layers are interconnected with formate bridges. In the second site, Mn2 ions are octahedrally coordinated with two bonds to formate oxygen atoms and four bonds to water oxygen atoms. These unlinked ions form separate layers that interpenetrate the layers formed by the Mn1 ions. The two

[a] Dr. R. D. Poulsen, M. R. V. Jørgensen, Dr. J. Overgaard, Prof. F. K. Larsen, Dr. W. Morgenroth, Prof. Dr. B. B. Iversen
Department of Chemistry
University of Aarhus
8000 Århus C (Denmark)
Fax: (+45) 8619-6199
E-mail: bo@chem.au.dk

[b] Dr. T. Graber, Dr. Y.-S. Chen
ChemMatCARS beam line, The University of Chicago
Advanced Photon Source, Argonne, IL 60439 (USA)

Supporting information for this article is available on the WWW under http://www.chemeurj.org/ or from the author.

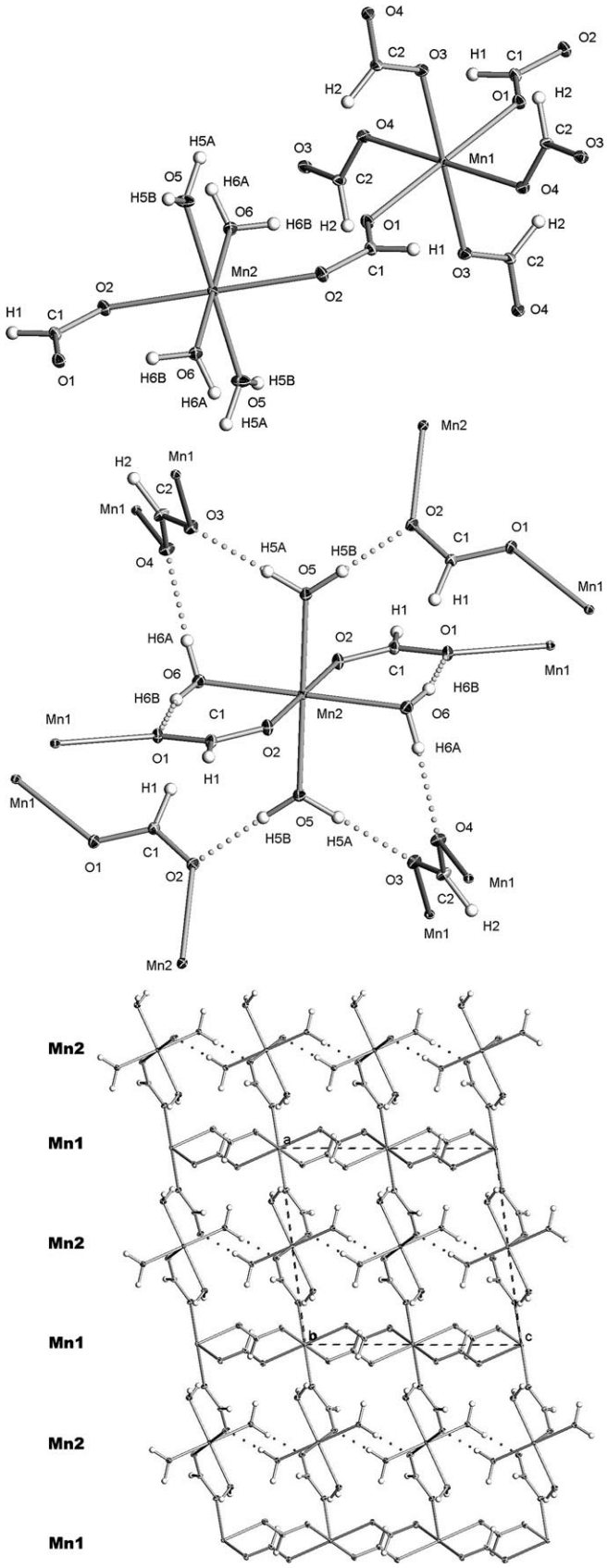

Figure 1. The crystal structure of $[Mn(HCOO)_2(H_2O)_2]_\infty$ (**1**) at 16(2) K with thermal ellipsoids at the 50% level. Top: The coordination around the metal sites. Middle: The hydrogen bonds. Bottom: the framework with alternating layers of Mn1 and Mn2 atoms.

types of layers are connected with direct formate bridges between Mn1 and Mn2. Thus, the Mn2 ions are isolated from each other, while the Mn1 ions are connected.

Isostructural frameworks are known for many 3d transition metals, and their physical properties have been studied using a wealth of methods. The manganese-containing framework exhibits particularly interesting magnetism, with at least three distinct phase transitions at 3.7, 1.7, and 0.6 K.[5] Since very large, high-quality crystals can be synthesized, it has been possible to study the structure by means of single-crystal polarized neutron diffraction (PND).[6] The measured spin density revealed that the 3.7 K phase transition is due primarily to antiferromagnetic ordering of the Mn1 ions, whereas the transition at 1.7 K is due to a reorientation of their spins. Below 1.7 K the Mn2 ions remain paramagnetic until a complete antiferromagnetic ordering of the structure occurs at 0.6 K. From the PND data the magnetic moments are estimated to be 0.38(2) μ_B on the Mn1 ions and 1.73(2) μ_B on the Mn2 ions.[6] Some spin density is observed on the linking formate groups with 0.1 μ_B transferred to oxygen atoms linked to Mn1 ions. This suggests that covalent bonding features are important for the magnetism, and it shows directly the involvement of the formate bridges in the magnetic superexchange mechanism.[6] It is, however, somewhat surprising that the formal high-spin Mn^{2+} ions show magnetic moments that are much smaller than the formal spin-only value of 5.92 μ_B. Curiously, we have not been able to find any literature references reporting estimates of the value of the magnetic moment based on magnetization measurements, and these have therefore been carried out in the present study. The isostructural Ni system has also been studied in detail.[7] In this system magnetic ordering is observed at 15.5 and 3.75 K. Zenmyo et al.[8] used proton NMR spectroscopy to probe the magnetic ordering in the Ni system, and modeling of the observed NMR resonances leads to estimates of the magnetic moments of 2.38 μ_B for the Ni1 ions and 0.38 μ_B for the Ni2 ions. The larger moment on the Ni1 ions in the Ni system relative to the Mn1 ions in the Mn system corroborates the higher ordering temperature of the M1 lattice, but it is intriguing why the relative size of the moments of the M1 and M2 sublattices are interchanged. This presumably is due to the chemical-bonding environment of the metal atoms, that is, covalent effects. For the Ni system magnetization measurements yield an effective moment of 3.14 μ_B,[7c] which is somewhat at variance with the NMR spectroscopic results. The comparison between the Mn and Ni systems shows that an understanding of the physical properties of the metal formate dihydrates must include detailed studies of the chemical bonding in the structures. Even though the different 3d metals yield isostructural crystals, the subtle details of the metal–ligand chemical bonding appear to change.

In a series of studies we have determined experimental charge-density (CD) distributions in manganese-based CPs.[9] Similar work has been carried out on copper-based CPs by Pillet and co-workers.[10] The basic idea has been to obtain a microscopic view of the electronic structure and

chemical bonding to supplement macroscopic information such as magnetization or heat capacity. Even though the CD does not explicitly contain information about the spin density, it allows a detailed study of the chemical bonding in the crystal, which is essential for understanding the magnetic pathways. Ultimately, the goal is to obtain a microscopic understanding of the macroscopic physical properties, since this is a prerequisite for the design of molecular magnets. In our previous studies the manganese-based CPs were structurally very complex with disordered solvent molecules.[9] This made determination of the experimental CD a great challenge in its own right, and the direct comparison of the results for different systems was somewhat hindered, since they were not completely isostructural. To better assess the results that can potentially be obtained with our approach we have chosen to use the methods on a simpler structure. The metal formate dihydrates are ideally suited for this purpose, and even though they are structurally relatively simple, they still have enough complexity, for example, with two unique metal centers, that CD information will constrain and challenge the understanding of their macroscopic properties. As described above, even the magnitude of the metal magnetic moments has not yet been properly understood. Furthermore, isostructural frameworks can be synthesized with a range of metals, providing a strong basis for comparative CD studies. To set a benchmark with which to compare future CDs, we use data sets measured at both synchrotron and conventional X-ray sources. The detailed comparison of these leads us to decide on the best CD for the present structure, and this is then subsequently used in analysis of the chemical bonding.

Results and Discussion

Physical properties: Figure 2 shows the magnetic susceptibility (χ) between 2 and 300 K. A fit of the data with $T>30$ K to the Curie–Weiss law ($\chi = C/(T-\Theta)+\chi_0$, in which $C = N\mu_0\mu_B^2\mu_{eff}^2/(3k_B)$, N is density of magnetic ions in the relevant units, μ_{eff} is the effective moment, Θ is the Weiss temperature, and χ_0 is a temperature independent term) gives $\Theta = -3.68(2)$ K, $\mu_{eff} = 5.840(2)\ \mu_B$ and $\chi_0 = -2.1(2)\cdot10^{-9}\ m^3\,mol^{-1}$. Thus, μ_{eff} is relatively close to the theoretical value of 5.9 μ_B for a free Mn^{2+} ion.[11] This, taken together with the negative Weiss temperature ($\Theta = -3.68$ K) and a linear magnetization with magnetic field at 300 K (inset in Figure 2) indicates antiferromagnetic ordering below 3.7 K in perfect agreement with previous studies of **1**.[5]

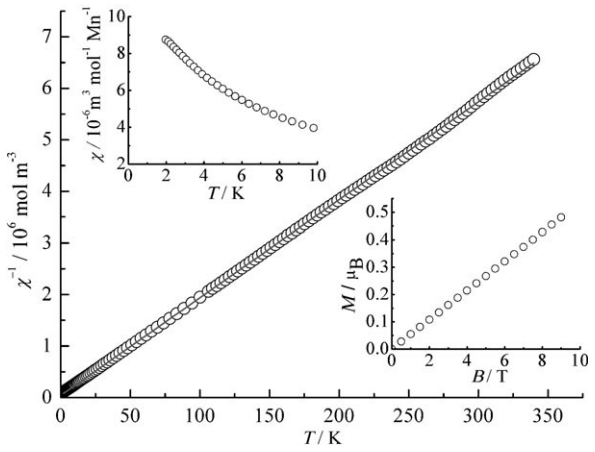

Figure 2. Magnetic susceptibility (χ) as function of temperature (T) measured in a magnetic field (B) of 2 T. The solid gray line is a Curie–Weiss modeling of $\chi(T)$ above 30 K. The upper inset shows the same data on linear scale in the low-temperature region. The lower inset shows the magnetization (M) as function of B measured at 300 K.

In Figure 3 the specific heat (C_p) as function of temperature is shown. A peak is observed below ≈10 K with a peak

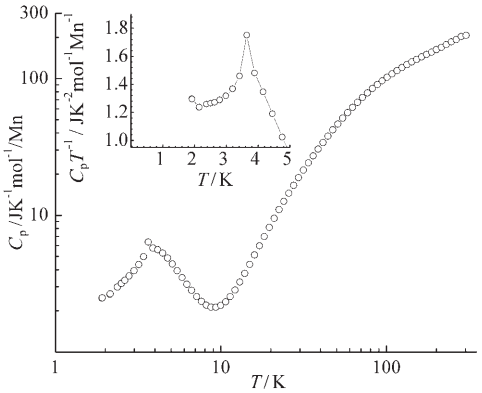

Figure 3. Specific heat (C_p) as function of temperature (T). The inset shows the same data plotted as C_p/T versus T.

maximum at approximately 3.7 K. From the inset of Figure 3, which shows C_p/T as function of T, we estimate the entropy change in the first phase transition to be approximately 6 $J\,K^{-1}mol^{-1}$ per Mn ($\Delta S = \int(\Delta C/T)dT$). This is in reasonable agreement with what can be expected from a magnetic ordering of half the high spin Mn^{2+} ions (Mn(1) lattice), with $J = 5/2$ and $\Delta S = {}^1/_2 R\ln(2J+1) = 7.5\ J\,K^{-1}mol^{-1}$.

X-ray data comparison: In Table 1 we list crystallographic data and details of multipole model refinement. The reduced structure factors on an absolute scale can be compared readily if anomalous dispersion and extinction effects are removed from the data, and provided that the data collection temperatures match. For the crystals used here, the refined extinction parameters were insignificant, and hence only the anomalous dispersion has been corrected for.

Figure 4 shows the ratio of structure factor amplitudes as a function of scattering angle between the two 100 K data sets. The common reflections comprise 5322 unique reflections out of 10522 (Hasylab) and 5539 (conventional) reflections used in the refinements. There is a pronounced tendency for the F(conventional)/F(Hasylab) ratio to decrease as the scattering angle increases. As expected, the spread increases significantly at higher scattering angle due to the reduced amplitude and the associated larger impact of the un-

Table 1. Crystallographic data and refinement details.

	Aarhus conventional	Hasylab synchrotron	APS synchrotron
formula	$Mn_2C_4H_{12}O_{12}$	$Mn_2C_4H_{12}O_{12}$	$Mn_2C_4H_{12}O_{12}$
M_r[g mol^{-1}]	724.03	724.03	724.03
crystal system	monoclinic	monoclinic	monoclinic
space group	$P2_1/c$	$P2_1/c$	$P2_1/c$
T [K]	100(2)	100(2)	16(2)
sample size [μm^3]	150×220×250	150×220×250	20×20×25
a [Å]	8.8080(4)	8.7940(13)	8.8263(1)[a]
b [Å]	7.2136(3)	7.2080(5)	7.2247(1)[a]
c [Å]	9.6203(4)	9.5940(8)	9.6305(1)[a]
β [°]	97.693(2)	97.664(7)	97.689(1)[a]
V [Å^3]	605.75(5)	602.70	608.59(2)[a]
λ [Å]	0.71073	0.550	0.413
Z	4	4	4
ρ_{calcd} [g cm^{-3}]	1.985	1.995	1.976
μ [mm^{-1}]	2.14	0.98	0.38
min/max transmission	0.82/0.77	N/A	1.00/0.99
integrated reflns	25061	180245	35107
unique reflns	7212 (all)	15080[b]	9326 (all)
			5189 ($n_{meas}>2$)
R_{int}	0.027	0.07	0.045
$\sin\theta/\lambda_{max}$ [Å^{-1}]	1.18	1.56	1.29
N_{par}	263	263	263
N_{obs}	5539 (1σ)	10522 (3σ)	3833 (2σ)
$R(F)$, $R(F^2)$	0.024, 0.024	0.036, 0.043	0.023, 0.025
$R_w(F)$, $R_w(F^2)$	0.017, 0.033	0.031, 0.060	0.021, 0.042
goodness-of-fit	1.23	1.67	0.57

[a] In the charge-density refinement of the APS data a unit cell of $a=8.809$, $b=7.199$, $c=9.619$ Å, $\beta=97.69°$, $V=604.5$ Å^3 was used. This cell was obtained from an unpublished 15 K single-crystal X-ray experiment.[12] [b] The data averaging led to 18698 unique reflections, which in many cases were extremely weak. The data set was "cleaned" for severe outliers using the refined multipole model. This was done by removing all data with $|F(obs)-F(model)|/\sigma(F(obs)>10$, $|F(obs)/F(model)|>5$ or $|F(obs)/F(model)|<0.2$. For a discussion of this procedure see Iversen et al.[13]

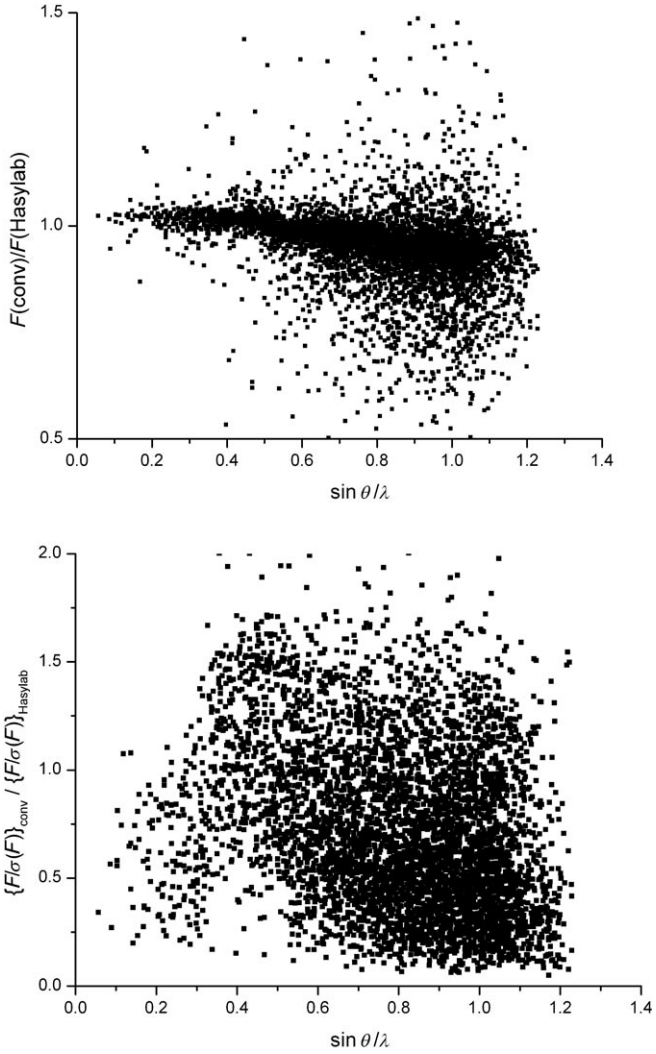

Figure 4. Top: Ratio of the common structure factors in the conventional and the Hasylab data corrected for anomalous dispersion. Bottom: The relative significance of the reflections, $[F_o/\sigma(F_o)]_{Conv}/[F_o/\sigma(F_o)]_{Hasylab}$), versus $\sin\theta/\lambda$.

certainty of the measurements. However, it is clear that a large proportion of reflections at higher angle have relatively lower amplitudes in the conventional data than in the Hasylab data. The bulk of the data suggest that the effect reaches a minimum of about 90%. One consequence of this is that the atomic displacement parameters (ADPs) become smaller in the Hasylab model relative to the conventional data model. On the other hand it is also clear that the low-order data are slightly stronger in the conventional data than in the Hasylab data. As seen in Figure 4 (bottom), the intense beam of the synchrotron has clearly produced more significant high-order data. The origin of the observed scattering-angle-dependent discrepancy in the structure factor amplitudes could be incomplete corrections for systematic errors.

Comparison of structural parameters: The positional parameters obtained from the three data sets are nearly identical, and as seen in Table 2 the corresponding bond lengths and bond angles agree well. The lowering of the temperature from 100 to 16 K has little influence on the crystal structure. In general the estimated standard deviations are larger for the APS structure (third line), showing that the precision of both the conventional data and the Hasylab data is better than the APS data. However, this does not reveal which structure is the most accurate.

On the other hand differences are observed between the ADPs, which are more delicate probes for the reliability of the data. In Figure 5 the relative values of the diagonal elements of the **U** tensor are displayed for the 100 K data sets. It is evident that the Hasylab ADPs are significantly smaller than the corresponding conventional ADPs. The 10–20% difference in ADPs illustrates the importance of systematic errors even in presumably accurate X-ray diffraction data. One may argue that the precise value of the ADPs is not important if the goal is the static electron density. In other words, if uncorrected systematic errors are completely absorbed in the ADPs, then the deconvolution of the thermal

Table 2. Bond lengths and angles. The first line is the 100 K conventional data, the second line the 100 K Hasylab data, and the third line the 16 K APS data.

	Length [Å]		Angle [°]
Mn1−O1	2.1967(5)	O1-Mn1-O3	92.50(2)
	2.1932(4)		92.51(2)
	2.1964(8)		92.63(3)
Mn1−O3	2.1764(5)	O1-Mn1-O4	92.40(2)
	2.1714(4)		92.42(2)
	2.1771(7)		92.39(3)
Mn1−O4	2.1546(5)	O3-Mn1-O4	89.56(2)
	2.1527(4)		89.61(2)
	2.1530(8)		89.45(3)
Mn2−O2	2.2251(6)	O2-Mn2-O5	89.94(3)
	2.2215(4)		90.02(2)
	2.2241(7)		90.03(3)
Mn2−O5	2.1570(6)	O2-Mn2-O6	92.36(2)
	2.1516(5)		92.38(2)
	2.1564(8)		92.37(3)
Mn2−O6	2.1978(5)	O5-Mn2-O6	89.92(2)
	2.1936(4)		90.03(2)
	2.1978(9)		90.04(4)
O1−C1	1.2619(7)	Mn1-O1-C1	129.62(4)
	1.2586(6)		129.62(3)
	1.2629(12)		129.65(6)
O2−C1	1.2540(7)	Mn2-O2-C1	132.91(4)
	1.2523(5)		133.00(3)
	1.2560(11)		132.82(7)
O3−C2	1.2523(7)	Mn1-O3-C2	125.29(4)
	1.2502(5)		125.26(3)
	1.2518(11)		125.25(6)
O4−C2	1.2589(7)	Mn1-O4-C2	121.27(4)
	1.2540(6)		121.29(3)
	1.2578(9)		121.26(6)
		O1-C1-O2	125.08(5)
			125.07(4)
			124.99(8)
		O1-C1-H1	117.52(5)
			117.49(4)
			117.51(7)
		O2-C1-H1	117.40(5)
			117.44(4)
			117.50(8)
		O3-C2-O4	124.59(5)
			124.55(4)
			124.56(8)
		O3-C2-H2	117.81(5)
			117.85(4)
			117.66(7)
		O4-C2-H2	117.59(5)
			117.57(4)
			117.78(8)

motion still leads to an accurate density model. In the following we therefore compare the static densities obtained from the three data sets in order to decide on the most accurate model. This density will then be used for further interpretation.

Comparison of electron density distributions: In charge-density studies, chemical bonding analysis is typically performed by using the topological approach of the quantum theory of atoms in molecules.[14] In Table 3 the bond critical points (bcp) located in the three densities are listed. The three

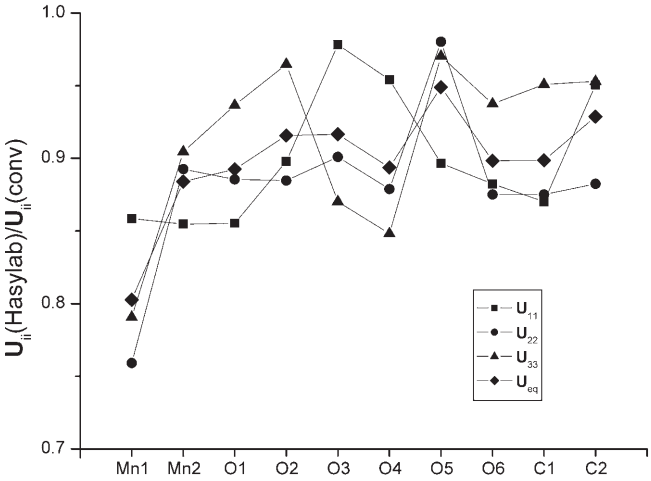

Figure 5. Relative values of the diagonal elements of the **U** tensor between the Hasylab and the conventional data measured at 100 K.

data sets lead to densities that overall have similar topological features, that is, the number and types of critical points are identical. When examining the topological measure it is clear that there is excellent agreement between the two densities derived from 100 K data (conventional and Hasylab), but that slightly different values are observed for the APS density. Thus, the APS density, for example, has slightly larger values of ρ_{bcp} in the metal–ligand bonds. The largest discrepancies are observed in the polar C–O bonds, in which the topological properties can be affected by the radial flexibility of the multipole model.[15] The APS model has larger positive curvatures at the bcp (i.e., λ_3) than the two 100 K densities, and this leads to smaller values of the Laplacian at the bcp. The position of the bcp in the C–O bonds is also affected, and for the APS density it is located farther from the oxygen atoms, leading to smaller values of ρ_{bcp}.

Recently, the development of a methodology for comparing theoretical molecular charge densities with the emphasis on improvement of QSAR-type studies was proposed by Popelier et al.[17] The method defines the different properties evaluated at the bond critical points as coordinates in an imaginary topological space, and compares these coordinates as one would do, for example, with positional coordinates in real space. The method condenses the comparison of the densities to a single number. In the present case we use ρ_{bcp}, $\nabla^2\rho_{bcp}$, and $d_{1\text{-}bcp}$ for the ten bonds (not including hydrogen atoms) of Table 3. Between the conventional density and the Hasylab density the comparison number is 1.75, between conventional and APS it is 4.15, and between Hasylab and APS it is 2.42. The values corroborate the fact that there is better agreement in topological space between the two 100 K-derived densities than in any comparison involving the APS density.

In summary, it is clear that the structures obtained with the conventional data and the Hasylab data at 100 K are more precise than the 15 K APS structure, and that the first two densities agree well with each other, but show some dis-

Table 3. Bond critical points in the static electron densities. ρ is the electron density [e Å^3], $\nabla^2\rho$ the Laplacian [e Å^5], d_{1-2} [Å] the sum of distances between the bcp and the atomic attractors, $d_{1\text{-bcp}}$ the distance [Å] from the first atom to the critical point, and λ_i the eigenvalues of the Hessian matrix at the bcp. G, V, and H are the kinetic energy density, the potential energy density, and the total energy density [hartree Å^{-3}] derived using the Abramov functional.[16] The random errors estimated from the least-squares procedure are typically on the third decimal for ρ and $\nabla^2\rho$. This is much smaller (by an order of magnitude) than the systematic error due to the specific choice of density model. Therefore, we only list the values to the second decimal in ρ and first decimal in $\nabla^2\rho$. The first line is the conventional data, the second the Hasylab data, and the third the APS data.

Bond	$\rho_b(r)$	$\nabla^2\rho(r)$	d_{1-2}	$d_{1\text{-bcp}}$	λ_1	λ_2	λ_3	G	V	H	G/ρ
Mn1−O1	0.27	6.6	2.197	1.094	−1.5	−1.4	9.5	0.40	−0.33	0.06	1.47
	0.28	6.5	2.193	1.092	−1.5	−1.5	9.5	0.40	−0.34	0.06	1.44
	0.31	6.8	2.197	1.083	−1.7	−1.6	10.0	0.43	−0.38	0.05	1.40
Mn1−O4	0.31	7.5	2.155	1.076	−1.7	−1.7	10.9	0.46	−0.40	0.06	1.50
	0.32	7.4	2.153	1.067	−1.8	−1.7	10.9	0.47	−0.41	0.06	1.47
	0.34	7.7	2.153	1.072	−1.9	−1.8	11.4	0.49	−0.45	0.04	1.44
Mn1−O3[a]	0.28	6.8	2.177	1.085	−1.5	−1.5	9.8	0.41	−0.35	0.06	1.47
	0.30	6.9	2.172	1.080	−1.6	−1.5	10.1	0.43	−0.37	0.06	1.45
	0.33	7.3	2.177	1.080	−1.8	−1.7	10.8	0.46	−0.42	0.05	1.42
Mn2−O2	0.24	5.8	2.225	1.103	−1.2	−1.2	8.3	0.34	−0.28	0.06	1.44
	0.25	5.9	2.222	1.101	−1.3	−1.3	8.5	0.36	−0.30	0.06	1.44
	0.28	5.9	2.225	1.113	−1.4	−1.4	8.7	0.37	−0.33	0.04	1.32
Mn2−O5	0.30	7.3	2.157	1.070	−1.7	−1.6	10.6	0.45	−0.39	0.06	1.49
	0.30	7.2	2.152	1.069	−1.7	−1.6	10.5	0.44	−0.39	0.06	1.47
	0.35	7.1	2.156	1.072	−1.9	−1.7	10.7	0.47	−0.44	0.03	1.36
Mn2−O6	0.27	6.5	2.198	1.089	−1.4	−1.4	9.3	0.39	−0.33	0.06	1.46
	0.27	6.6	2.194	1.090	−1.5	−1.4	9.5	0.40	−0.34	0.06	1.46
	0.31	6.6	2.198	1.097	−1.6	−1.6	9.8	0.42	−0.38	0.04	1.36
O1−C1	2.80	−33.8	1.262	0.799	−26.1	−22.9	15.2				
	2.70	−24.7	1.259	0.835	−25.0	−22.6	22.9				
	2.50	−4.3	1.264	0.853	−21.1	−20.3	37.1				
O2−C1	2.77	−34.1	1.254	0.768	−25.3	−22.7	13.9				
	2.64	−20.9	1.253	0.833	−24.2	−22.6	25.9				
	2.42	−4.0	1.256	0.844	−20.0	−19.1	35.1				
O3−C2	2.91	−37.7	1.252	0.781	−27.2	−24.8	14.2				
	2.71	−20.5	1.251	0.831	−23.8	−23.0	26.3				
	2.53	−3.3	1.252	0.844	−22.7	−20.6	40.1				
O4−C2	2.75	−31.8	1.259	0.793	−25.1	−22.1	15.4				
	2.65	−19.4	1.254	0.835	−23.6	−22.7	26.8				
	2.36	−3.6	1.258	0.842	−18.8	−18.4	33.6				
O5−H5A	2.27	−33.1	0.990	0.766	−35.2	−34.4	36.5				
	2.21	−29.5	0.990	0.766	−33.8	−33.2	37.5				
	2.35	−30.6	0.990	0.747	−34.1	−32.6	36.2				
O5−H5B	2.22	−27.2	0.990	0.758	−33.1	−32.4	38.4				
	2.19	−23.5	0.990	0.752	−31.9	−30.6	39.0				
	2.15	−22.8	0.990	0.755	−31.3	−29.7	38.2				
O6−H6A	2.28	−28.4	0.990	0.751	−33.3	−32.7	37.6				
	2.25	−22.9	0.990	0.734	−30.8	−30.1	37.9				
	2.23	−26.1	0.990	0.752	−32.0	−31.2	37.1				
O6−H6B	2.38	−28.1	0.990	0.747	−34.9	−33.6	40.4				
	2.25	−24.5	0.990	0.758	−33.2	−32.9	41.5				
	2.24	−21.7	0.990	0.749	−31.9	−30.8	41.0				
C1−H1	1.71	−16.8	1.084	0.785	−18.8	−17.3	19.2				
	1.71	−16.3	1.084	0.794	−18.1	−16.6	18.5				
	1.70	−15.0	1.084	0.757	−16.4	−15.0	16.5				
C2−H2	1.63	−16.2	1.084	0.791	−17.9	−16.7	18.3				
	1.66	−15.4	1.084	0.794	−17.4	−16.1	18.0				
	1.68	−16.9	1.084	0.750	−16.2	−14.8	14.1				
O5−H5A···O3[a]	0.12	4.9	1.787	1.208	−0.6	−0.6	6.0	0.25	−0.16	0.09	2.09
	0.16	4.4	1.782	1.188	−0.8	−0.8	6.0	0.24	−0.18	0.07	1.56
	0.13	5.1	1.786	1.205	−0.6	−0.6	6.3	0.27	−0.18	0.09	2.01
O5−H5B···O2[b]	0.18	4.8	1.756	1.169	−1.0	−1.0	6.7	0.27	−0.20	0.07	1.53
	0.20	4.8	1.750	1.161	−1.1	−1.1	7.0	0.28	−0.22	0.06	1.40
	0.24	4.7	1.756	1.169	−1.4	−1.4	7.4	0.29	−0.26	0.04	1.22
O6−H6A···O4[c]	0.13	4.8	1.782	1.192	−0.7	−0.6	6.1	0.25	−0.17	0.09	1.93
	0.15	5.0	1.775	1.187	−0.8	−0.7	6.5	0.27	−0.18	0.08	1.82
	0.18	4.6	1.777	1.182	−0.9	−0.9	6.4	0.26	−0.20	0.06	1.45
O6−H6B···O1[d]	0.16	4.1	1.834	1.189	−0.9	−0.8	5.8	0.23	−0.17	0.06	1.43
	0.20	3.9	1.815	1.173	−1.1	−1.1	6.1	0.24	−0.20	0.04	1.19
	0.23	4.0	1.809	1.168	−1.3	−1.2	6.5	0.26	−0.24	0.02	1.10

[a] $x, y+1, z$. [b] $-x+1, y+0.5, -z+0.5$. [c] $-x+1, -y, -z$. [d] $-x+1, -y+1, -z$.

crepancy in the finer density details with the APS density. Does this mean that the two "100 K" densities are more trustworthy?

In Figure 6 static deformation densities in selected ligand planes are shown. The static deformation density is the difference between the multipole model density and the density of a promolecule model (superposition of free spherical atoms). Corresponding plots of the Laplacian distribution are shown in the Supporting Information. The static deformation plots reveal subtle differences between the models. It is most straightforward to analyze deformation densities of the ligands, since to a large degree they should show the expected features of such functional groups. When looking at the water and formate groups it is clear that both the conventional and the Hasylab data have more pronounced and symmetric oxygen lone-pair densities, as well as larger mid-bond deformation densities. However, the most striking difference is that the APS deformation density shows distinct negative areas near the oxygen nuclei in both the formate and the water groups (Figure 6) as well as on both the metal sites (see the Supporting Information). While it is not clear how the metal sites are "expected" to look in **1**, it is straightforward to compare the water deformation density with a high-quality theoretical calculation on the isolated water molecule. This has been presented frequently in the literature,[18] and theoretical calculations clearly show negative density around the oxygen center and positive density in the hydrogen region. The same deformation features have been observed in very high accuracy experimentally derived static deformation densities of metal-coordinated water molecules.[18] The similarity between the APS density and the expected static deformation density for water is striking, whereas the two 100 K derived densities are different. The comparison gives strong support that the APS density is the most accurate. It is worth noting that the conclusions of the density reliability are unchanged if we use exactly the same subset of structure factors in the three multipole refinements. In other words the model densities are not different due to differences in the data resolution between the three data sets.

The relatively lower accuracy of the present 100 K derived densities could be due to an improper deconvolution of the thermal motion. If there are correlations between the ADPs and the electron density parameters, the static deformation density will be affected. This is likely to be evident from the dynamic deformation density maps of the sections shown in Figure 6, since the dynamic deformation density function is calculated as a Fourier summation of the structure factor differences, thereby inherently including the thermal effects. Such maps for selected planes are shown in the Supporting Information. The deformation features in the dynamic maps are much decreased compared with the static deformation density maps, but overall the dynamic maps are similar to the static counterparts. Clearly, the negative regions on the oxygen nuclei are present in the APS dynamic deformation density, but absent in the conventional and Hasylab densities. The negative feature therefore does not seem directly related to an improper deconvolution, but has a more subtle origin.

Another conspicuous feature in the static deformation densities of the 100 K derived maps is a tendency for double peaks in the O–H water bonds. This feature presumably is related to slightly erroneous radial κ values. In fact, it seems that if a spherical density component is subtracted at some distance from the oxygen nuclei in the 100 K derived maps, the features will look more similar to the APS density and the theoretical density. The refined oxygen κ parameters are 0.999(1) for the conventional data, 0.993(2) for the Hasylab data and 0.963(2) for the APS data. New refinements were carried out on the conventional and the Hasylab data with κ values fixed to the values obtained in refinement of the APS data. The corresponding static deformation densities of the water ligands are shown in Figure 7. It may be noted that for the oxygen atom in water molecules, a κ value of 1.00 has been suggested in the κ-restricted procedure advocated by Coppens et al., based on multipole refinement against theoretical structure factors.[19] This is similar to the value found in the 100 K refinements. Nevertheless, the conventional data and the Hasylab data give static deformation maps for water much closer to theoretical results when a κ value of 0.963 is used as obtained in refinement of the APS data.

Deformation features close to the nuclei are sensitive to small changes in the scale factor. To find the source of a potentially small scale factor and/or κ parameter error in the 100 K data sets, we have compared the observed structure factors with the model structure factors in each data set, as in Figure 8.

In the conventional data there is a clear tendency for $F(\mathrm{obs})/F(\mathrm{model})$ to decrease for the high-order data, and thus these data have a different scale factor than the low-order data. The Hasylab data have a slightly "oscillatory"-scale factor through the data set. On the other hand Figure 8 nicely illustrates that the APS data have a constant-scale factor for both high- and low-order data, suggesting that systematic errors are reduced for this data set.

What may be the systematic errors that lead to the slight deterioration of the two 100 K data sets compared with the 16 K data set? If we compare the two 100 K data sets, they are indeed collected under very different experimental conditions. One uses conventional $Mo_{K\alpha}$ radiation with a Bruker APEXII CCD detector, whereas the other uses short wavelength synchrotron radiation and a MAR165 CCD detector. The diffractometer geometries are also different for the two 100 K experiments, and the software used to integrate and process data is different. All these features are different again in the APS data, for which yet another geometry, detector, and software is used. Even so the two 100 K data sets lead to similar model densities. It seems likely that the systematic error must come either from the change in temperature or the fact that the APS data collection used a much smaller crystal. The crystal size affects systematic errors such as extinction and absorption, and in the APS data these effects are for all practical purposes re-

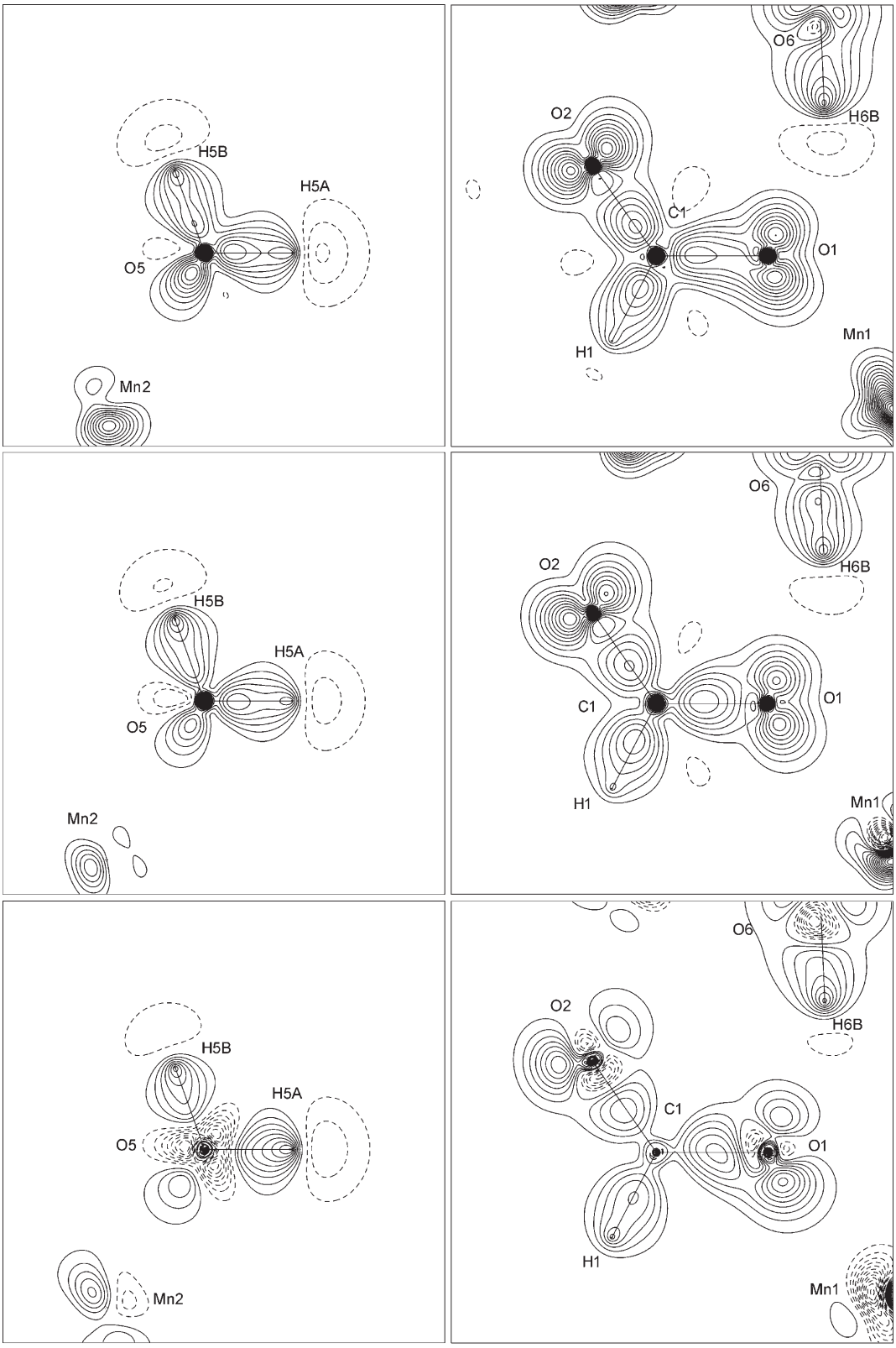

Figure 6. Static deformation density maps for selected ligand planes. The top two maps represent the conventional model, the middle two the Hasylab model, and the bottom two the APS model. The contour interval is 0.1 e Å^{-3}. Positive contours are solid lines and negative are dashed lines. The zero contour is not shown.

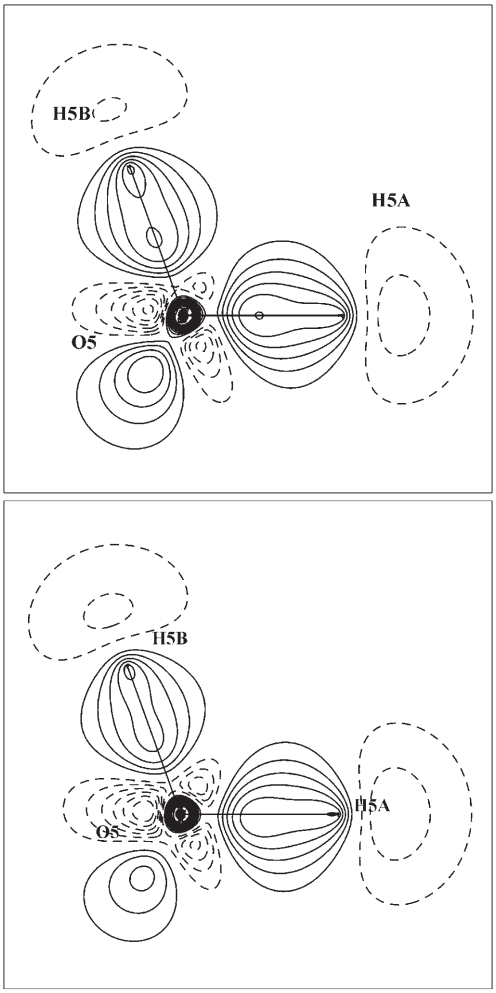

Figure 7. Static deformation density maps for the water plane with κ for all atoms fixed to the values obtained in refinement of the APS data. The top plot is for the conventional model, and the bottom one is for the Hasylab model. The contour level is 0.1 e Å^{-3}. Positive contours are solid lines and negative are dashed lines. The zero contours are not shown.

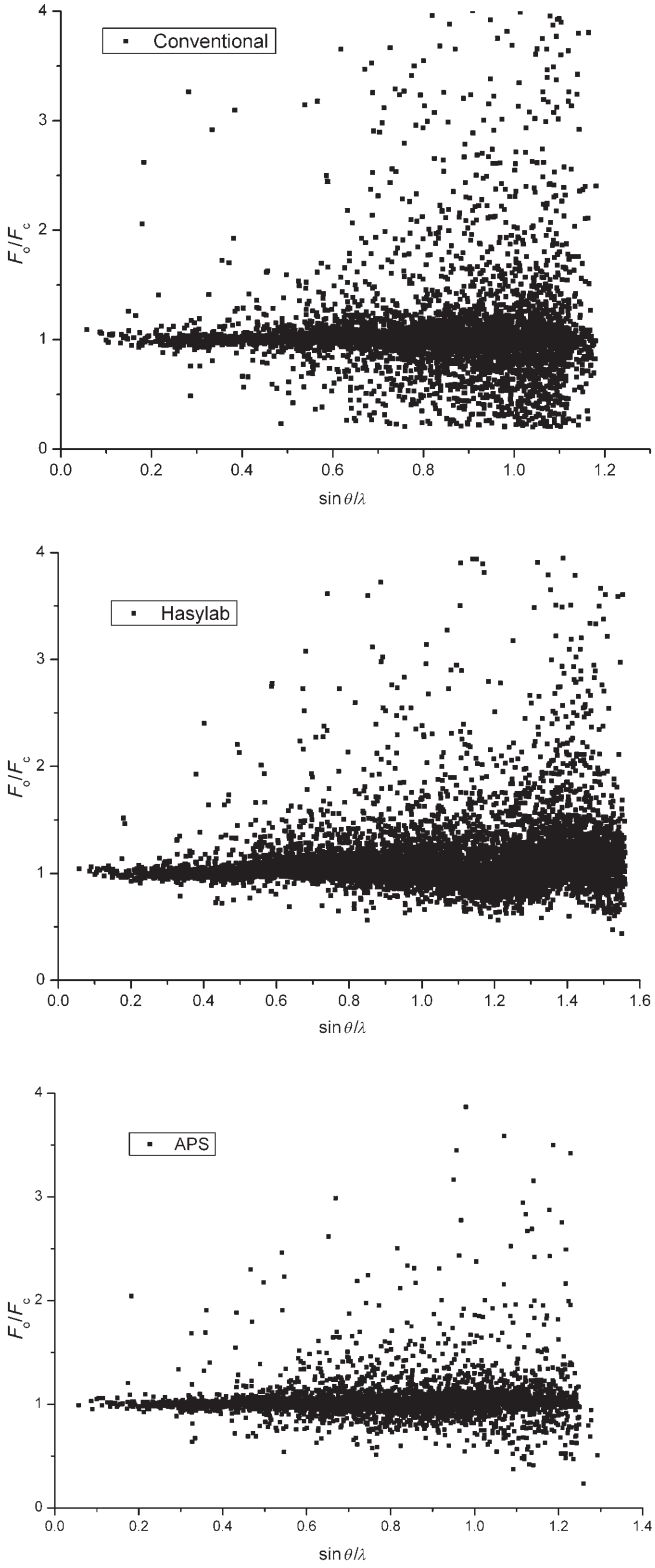

Figure 8. F(obs)/F(model) versus $\sin\theta/\lambda$ for the conventional data (top), the Hasylab data (middle), and the APS data (bottom).

moved. However, none of the refinements observed significant extinction parameters, and the maximum and minimum absorption corrections for the longer wavelength conventional data set are 77% and 82%, respectively. Thus, a potential error in this correction is presumably below ≈1%. If absorption is the source of the error it would be quite a coincidence that the two 100 K data sets retrieve such similar densities, especially considering that the correction is quite different for the two data sets. Overall, it therefore seems that the error at least partially relates to the temperature difference between the studies. The major temperature-dependent systematic errors in diffraction data are thermal diffuse scattering (TDS) and anharmonicity. We included anharmonic Gram–Charlier parameters in refinements of all three data sets, but in all cases they were insignificant. This leaves just TDS. As discussed by Iversen and co-workers in a number of studies, TDS corrections can be quite large even for hard inorganic substances with high Debye temperatures.[20] Thus, for metallic Mg (θ_D = 330 K) the TDS contribution to the scattered neutron intensity already at 0.8 Å^{-1} amounts to ≈10% at 125 K.[20a] We cannot at this point fully pinpoint the source of systematic errors in the two 100 K

data sets, but we can conclude that it is likely to be at least partly a temperature effect. The present study therefore gives yet another demonstration of the advantages gained in accurate diffraction experiments at 16 K rather than at 100 K.[21] Here, we merely conclude that the 16 K APS data have produced the most accurate density, and this density is used for further analysis of the system.

Chemical bonding: In the following, all discussion of the density features refers to the 16 K APS multipole model. Figure 9 shows static deformation densities in planes that go through the metal atoms. The deformation features on the two metal ions are not greatly different at a qualitative level of comparison. This means that the crystal environment affects the two formal Mn^{2+} ions in a similar way. For the Mn1 site one would expect that the axis pointing towards O1 is unique, since this is the bond connecting the Mn1 layers with the Mn2 ions (Figure 1, top). Presumably, this axis is also unique for the Mn2 site (i.e. Mn2···O2), since the perpendicular plane contains four water ligands. However, the deformation density features in the O3···Mn1···O4 plane appear to be quite similar to the features of the O6···Mn2···O3 plane (Figure 9, top). Thus, for Mn2 the unique axis may be towards the water O5 atom rather than the formate O2 oxygen.

What makes O5 special? For the O6 water atom the two hydrogen bonds are formed with formate oxygen atoms bonded to Mn1, whereas for O5 one hydrogen bond is "inside" the Mn2 layer and bound to O2 through H5B. This hydrogen bond is the strongest of the four listed in Table 3, and the Mn2···O5 axis is also the shortest metal–ligand bond. These are subtle indications that important chemical interactions are present in the Mn2 layer through the O5···H5B···O2 hydrogen bond, and it may be that these interactions also are important for the antiferromagnetic ordering of Mn2 at 0.6 K. Overall, it is clear that both metal sites have nonspherical deformation features. Since a high-spin Mn^{2+} ion is spherical, subtraction of a spherical reference density should give spherical deformation features. Thus the nonspherical features must originate from uneven occupancy of the d orbitals, and the metal sites cannot merely be regarded as high-spin Mn^{2+} ions. The features in Figure 9 reflect the orbital interactions that also mediate the magnetic ordering.

The shape and topology of the atomic densities can be visualized by plotting the Laplacian of the density at some (small) density isosurface, as shown in Figure 10. Clear valence-shell charge concentrations (VSCC), that is, minima in the $\nabla^2\rho$ valence shell, are found in between the metal–ligand bonds (red areas) reflecting the nonspherical nature of both Mn sites. In a topological sense the metal–ligand bonds are formed between ligand lone-pair concentrations and metal-charge depletions. The exact positions and density features of the VSCC are listed in the Supporting Information.

From the refined multipole populations one can derive experimental 3d orbital populations on the metal sites, as given in Table 4.[22] The derivation neglects orbital hybridization and covalent effects, that is, the odd-order multipoles are neglected, and the multipolar functions on different atoms are assumed to be non-overlapping. In the present case both Mn sites have inversion symmetry, so odd-order multipoles are forbidden anyway. It is worth noting that the two 100 K model densities lead to similar values of the d-orbital populations compared with the APS model (see Supporting Information). This is especially true when one is comparing relative occupancies (in %). The absolute values of the orbital populations are affected by the scale factor through the explicit dependence on the refined monopole populations. Thus, differences in these values may mask the fact that the anisotropies of the metal densities are similar. The virtually uniform d-orbital population parameters, especially on Mn2, are not really compatible with the anisotropy seen in Figure 9. This is even more apparent when considering that the metal deformation densities are quite different for the three different data sets, even though the derived orbital populations are similar (see Supporting Information). Thus, the extracted d-orbital populations appear rather insensitive to changes in the static deformation features. However, the bonding deformation features are not located along the metal–ligand bond axes, and they must therefore be described by orbital mixing terms. While axes definitions are usually clear for high-symmetry metal sites, it is not straightforward to decide on the optimum choice of local coordinate system (LCS) for low-symmetry sites. Sabino and Coppens have proposed that the "natural" choice of LCS for low-symmetry sites is the LCS that minimizes orbital cross terms.[23] In Table 4 we list orbital populations in the natural LCSs as calculated with program ERD,[23] while the Supporting Information contains a plot of the natural LCSs superimposed on a structural drawing. In the natural LCSs there are larger differences among the orbital populations for both metal sites in agreement with the static deformation density.

The orbital populations in Table 4 suggest that there is some donation from the ligands into the 3d orbitals compared with a high-spin Mn^{2+} ion, but that it is rather limited.

Table 4. Experimental d-orbital populations. The numbers in parentheses are percentages of the total number of d electrons. The Mn1 atom has *x* towards O4 and *y* towards O1, whereas Mn2 has *x* towards O5 and *y* towards O6. The third and fourth rows of data for each atom give the orbital populations in the local coordinate system obtained by minimization of orbital cross terms using the program ERD.[23]

	$d_{x^2-y^2}$	d_{z^2}	d_{xy}	d_{yz}	d_{xz}	SUM	Max. unpaired
Mn1	1.12	1.19	1.09	0.92	0.91	5.23	4.77
	(21.5)	(22.7)	(20.8)	(17.6)	(17.4)		
	0.91	1.32	0.91	1.25	0.84	5.23	4.77
	(17.4)	(25.2)	(17.4)	(23.9)	(16.1)		
Mn(2)	1.06	1.11	1.07	1.07	1.02	5.32	4.68
	(19.8)	(20.9)	(20.0)	(20.1)	(19.1)		
	0.89	1.37	0.89	1.26	0.92	5.32	4.68
	(16.7)	(25.7)	(16.8)	(23.6)	(17.3)		

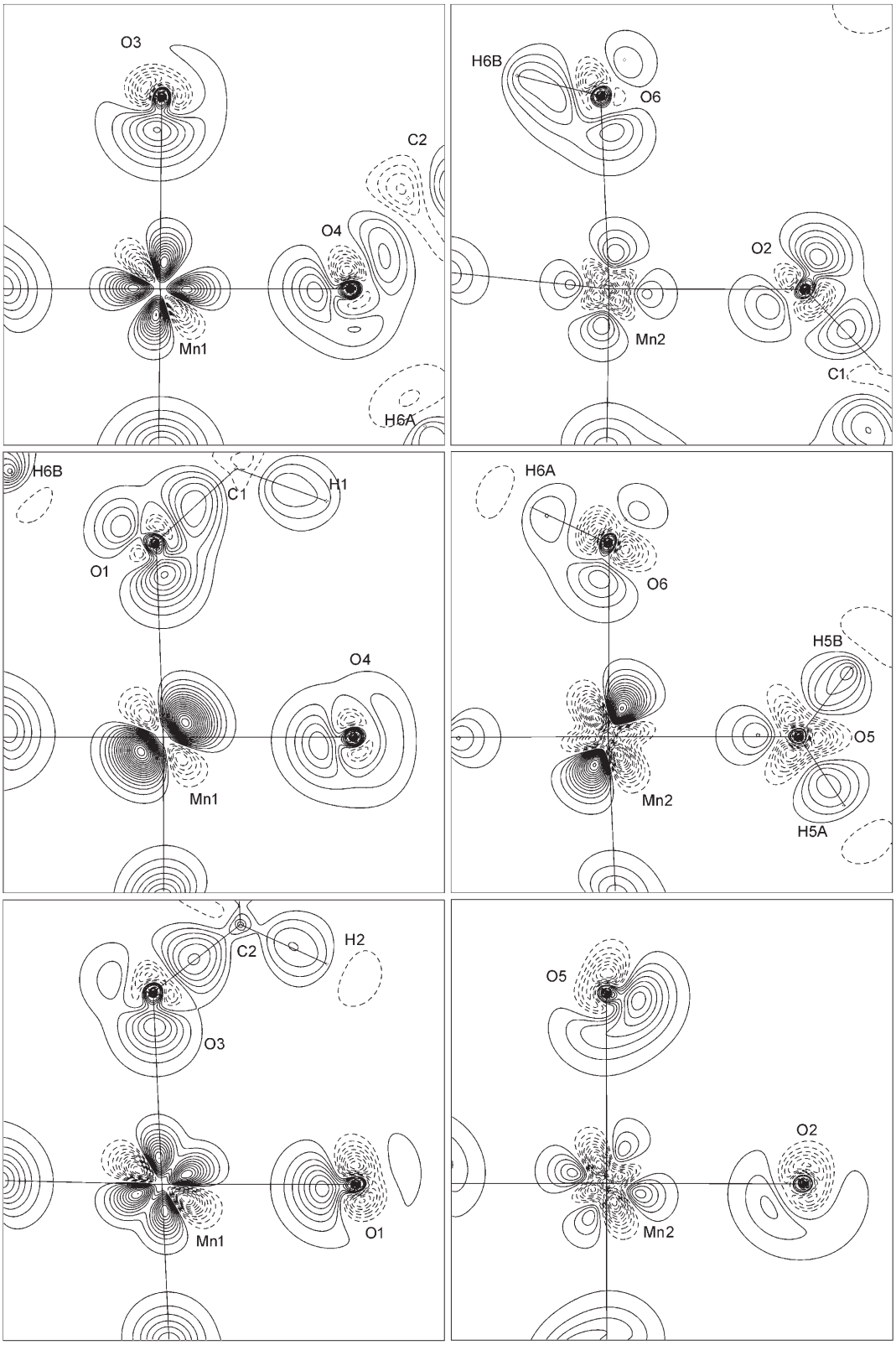

Figure 9. Static deformation density maps calculated from the 16 K multipole model, showing the Mn1–ligand planes (left-hand side), and Mn2–ligand planes (right-hand side). The contour level is 0.1 e Å^{-3}. Positive contours are solid lines and negative are dashed lines. The zero contour is not shown.

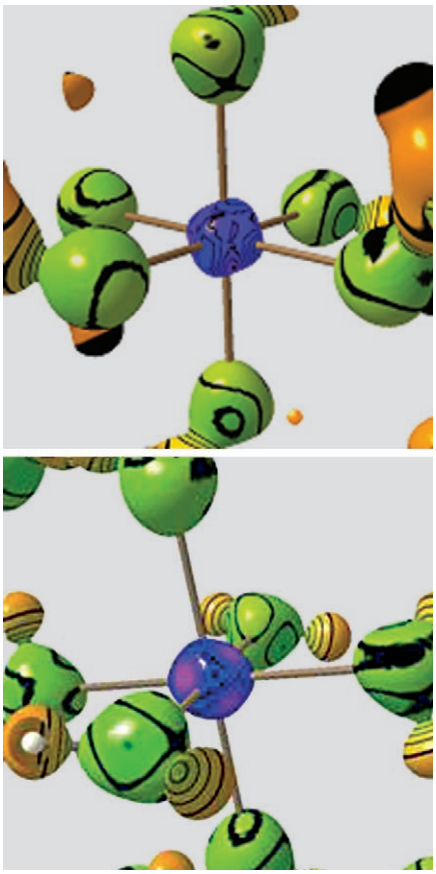

Figure 10. Laplacian distribution on the isosurface constituted of a value of the electron density of 0.01 e Å^{-3}. Red area shows charge concentrations. The color coding scheme is indicated in the Supporting Information. Top: Mn1. Bottom: Mn2.

Table 5. Atomic charges, atomic volumes, and dipole and quadropole (Q_{xx}, Q_{yy}, Q_{zz}) moments. All numbers are in atomic units. The moments refer to a global orthogonal Cartesian coordinate system.

Atom	P_Ω	V_{001}	Dipole moment	Quadrupole Moments
Mn1	1.68	66.8	0.0	−5.52, −5.43, −5.54
Mn2	1.60	71.2	0.0	−5.67, −5.74, −5.77
O1	−1.30	107.3	0.6	−4.69, −4.58, −4.91
O2	−1.19	107.0	0.5	−4.52, −4.52, −4.79
O3	−1.30	105.2	0.6	−4.57, −4.84, −4.62
O4	−1.25	104.1	0.5	−4.60, −4.60, −4.61
O5	−1.09	127.8	0.3	−4.55, −5.03, −4.56
O6	−1.07	127.4	0.2	−4.59, −4.58, −4.82
C1	1.56	49.0	1.1	−1.17, −1.90, −2.22
C2	1.56	52.2	1.2	−2.06, −2.02, −1.42
H1	0.14	46.3	0.2	−0.51, −0.36, −0.52
H2	0.29	34.8	0.1	−0.28, −0.36, −0.36
H5A	0.54	13.8	0.1	−0.17, −0.19, −0.14
H5B	0.51	16.3	0.1	−0.08, −0.16, −0.15
H6A	0.53	15.4	0.1	−0.15, −0.15, −0.15
H6B	0.44	19.1	0.1	−0.23, −0.13, −0.24

The d-orbital populations support the conclusion that to a first approximation one may regard *both* metal sites as high-spin Mn^{2+} ions, although it is the covalent interactions that are responsible for the magnetic ordering. It is conspicuous that the spin density obtained from polarized neutron diffraction gave values of the magnetic moments that are much smaller than the expected ionic values, and very different for the two Mn sites.[6] Even though the electron density does not contain explicit information on the spin distribution, the similarity between the experimental d-orbital populations and those expected for a free Mn^{2+} ion is clear. Considering that the effective moment derived from the magnetization measurements is close to the value obtained from five unpaired spins (5.840(2) μ_B), the present results appear to be at variance with the measured spin density. From the experimental orbital populations we can only estimate the maximum difference in alpha and beta spin, which for both metals is ≈4.7 electrons. Some of the magnetic moment is likely to be located in the ligand system, as shown by the polarized neutron diffraction measurements,[6] but it seems difficult to obtain almost 6 μ_B in effective moment if the majority spin is not located at the metal sites.

In Table 5 we list the atomic charges as defined by the zero-flux boundary condition.[14] Values from the two 100 K data sets are given in the Supporting Information. The cationic picture of the metal ions is supported by the atomic charges, which are similar at +1.68 and +1.60. These values are significantly different from the formal +2 value due to electron donation from the oxygen atoms. The nonspherical density features seen in Figures 9 and 10 are also reflected in the substantial manganese quadrupole moments. The oxygen charges range between −1.07 and −1.30 e, leading to quite positive carbon atoms at +1.56 e. The oxygen atoms have substantial dipole as well as quadrupole moments, and the carbon atoms are strongly polarized with large dipole moments. Among the hydrogen atoms there is a clear difference between formate and water hydrogen atoms. The water hydrogen atoms have charges of about +0.5 e, whereas the formate hydrogen atoms have smaller charges of +0.25 e. This may reflect the fact that the water hydrogen atoms are involved in hydrogen bonds where significant charge reorganization takes place.

We now turn to the topological measures at the bcps. All the metal–ligand interactions have positive values of $\nabla^2\rho$, positive values of the total energy density, and quite large values of G/ρ. This indicates that the chemical bonding is predominantly of closed-shell type. There are only small differences between the Mn···O(water) and Mn···O(formate) bonds, with the water ligands being slightly more strongly bonded. All the covalent bonds show the expected topological features with negative $\nabla^2\rho_{bcp}$ and high values of ρ_{bcp}. In particular the carboxyl groups appear to be completely delocalized, with very similar C–O bonds. The four quite strong hydrogen bonds (HB) in the structure are all between water O–H groups and formate oxygen atoms. The topological measures for the four HBs are also listed in Table 3. It requires data of high quality to correctly describe the weak intermolecular interactions, and the HBs show the same tendency as the topological analysis where the APS model gives significantly higher ρ_{bcp} values.

It is important to stress that the ionic bonding picture is only a first approximation. The fact that the structure has an antiferromagnetic ordering at low temperature suggests that there is significant metal–ligand orbital interaction. The Mn1···Mn1 distance is 6.020 Å, and the ordering must be indirect, occurring through a superexchange mechanism. It is difficult to see evidence in the experimental charge density that supports the two metal sites having very different magnetic moments. Both Mn atoms appear to be high-spin cations with charges of about +1.65. This is corroborated by the effective magnetic moments derived from magnetization measurements. The fact that the Mn1 lattice orders before the Mn2 lattice must be related to the Mn1 lattice being connected by formate bridges, whereas the Mn2 lattice involves water ligands and possibly the O5···H5B···O2 hydrogen bond. The Mn2 layers do not have the delocalized π system of the formates, which is probably a better mediator of the magnetism than the hydrogen bond. Further investigations of potential metal interactions with the formate π system will be carried out when densities on isostructural compounds are available (especially the nonmagnetic Zn compound).

Conclusions

The study has presented three different high-quality single-crystal X-ray diffraction data sets measured under very different conditions and processed using different software codes. The first is a conventional 100 K $Mo_{K\alpha}$ data set, the second a very high resolution 100 K data set measured on a second-generation synchrotron source, while the third is measured by using a tiny crystal on a high-brilliance third-generation synchrotron source at 16 K. All data sets have a quality that justifies multipole modeling of the charge density. The atomic positions, and thus bond lengths and angles, are very similar for all three data sets. On the other hand the ADPs of the two 100 K data sets differ by 10–20%, and there is a theta-dependent systematic difference between the two sets of structure factors. Oblique correction based on measured transmission factors is introduced for the large MAR165 CCD and it reaches up to 20% intensity correction with 0.55 Å radiation. On a charge-density level the two 100 K data sets agree well with each other, but show small differences to the 16 K data set. The most pronounced difference is the negative region near the oxygen nuclei in the 16 K static deformation density. Comparison with static deformation densities of isolated water molecules obtained from ab initio theory, and very accurate experimental static deformation densities of metal-coordinated water molecules, lead to the conclusion that the 16 K APS data set provides the most accurate density. The 16 K APS data set also has a more uniform scale factor throughout the data compared with the two 100 K data sets. The improvement in accuracy appears to be at least partly related to the lowering of the temperature, and possibly stems from reducing uncorrected thermal diffuse scattering effects.

Topological analysis of the metal–ligand bonding, and experimental 3d orbital populations on Mn atoms as well as Bader atomic charges indicate quite ionic high-spin metal atoms. The experimental charge density is therefore at variance with earlier spin density measurements, which reported low and very dissimilar magnetic moments on the metals. On the other hand, the charge density is supported by the effective moment estimated from magnetization measurements (5.840(2) μ_B). The magnetic ordering observed in the present study at 3.7 K, as well as in many earlier studies, must originate from a superexchange mechanism involving the formate ligands. Thus, covalent bonding effects are important, although subtle. Clear indications of non-ionic effects are seen in the static deformation density maps, where the metal atoms are nonspherical. The nonspherical nature of the metal charge distributions is reflected in the atomic quadrupole moments as well as in plots of the valence-shell charge concentrations (VSCC). The VSCC are located in between the metal–ligand bond directions. Overall, the present study has provided a benchmark charge density which can be used in comparison with future charge densities on hydrated metal formate framework structures.

Experimental Section

Synthesis: The synthesis of the metal–organic framework $[Mn_2(CHO_2)_4(H_2O)_4]_\infty$ (**1**) can be carried out in several ways. A simple route is to mix manganese acetate (500 mg) with water (2 mL), ethanol (3 mL), and formic acid (2 mL). This produces nice crystals after 72 h by diffusion. Alternatively, **1** can be synthesized as a decomposition product, when mixing of benzene-1,4-dicarboxylic acid (H_2BDC; 1.661 g, 10 mmol), diethyl formamide (DEF; 60 mL) and $Mn(NO_3)_2{\cdot}6H_2O$ (2.870 g, 10 mmol) dissolved in DEF (20 mL) in an autoclave. The autoclave was kept at 375 K for three days, yielding colorless, cubic crystals, which are not sensitive to the atmosphere. The solvothermal synthesis batch additionally contained minute colorless plate-shaped crystals of an unknown crystal phase.

Physical properties: The magnetic susceptibility (χ) and the total heat capacity (C_p) were measured on a Quantum Design PPMS system at the Department of Chemistry, University of Aarhus, from 2 to 300 K on a pellet pressed from finely ground powder. The material was found to be almost phase pure by conventional X-ray powder diffraction (see Supporting Information). The magnetic susceptibility was measured in a magnetic field of 2 T.

16(2) K single-crystal synchrotron X-ray data: A minute, colorless single crystal (0.020×0.020×0.025 mm) was mounted in protective oil on a glass fiber rod glued to a small copper wire. This assembly was mounted on a brass pin, which was placed on the goniometer of a HUBER four-circle diffractometer at the ChemMatCARS beamline at the Advanced Photon Source, Argonne National Laboratory, USA. The crystal was cooled to 16(2) K by using a cold He stream from a Pinkerton type cooling device.[24] The data collection was done in ϕ-scan mode with fixed ω and χ angles. The diffracted intensities were recorded with a Bruker R6000 CCD detector mounted on the 2θ arm of the diffractometer up to a maximum $\sin\theta/\lambda$ of 1.29 $Å^{-1}$. The intensities were integrated using SAINT+[25] and subsequently corrected for ϕ-dependent systematic errors based on equivalent reflections, and for the effect of oblique incidence of the X-rays into the detector surface by using locally developed software.[26] The intensities were then corrected for absorption from the multi-scan option available in SORTAV,[27] based on multiple measured intensities. SORTAV was also used to average equivalent reflections. The integration of the data resulted in a refined unit cell that was larger than

the 100 K unit cells reported below. The larger unit cell is in contradiction with the 15 K neutron diffraction unit cell reported in the literature.[6] We therefore believe that the larger unit cell is a nonphysical result, caused by a slight error in the wavelength. For this reason the APS data were subsequently refined by using unit cell parameters obtained from unpublished 15(2) K single-crystal X-ray diffraction data.[13]

100 K single-crystal synchrotron X-ray data: A colorless crystal of size $0.15\times0.22\times0.25$ mm was mounted with glue on a glass fiber and attached to a goniometer head using a tiny piece of copper wire and a brass pin. It was placed on a Huber four-circle diffractometer with a large offset Eulerian cradle (400 mm inner diameter) positioned in vertical diffraction geometry, installed at beamline D3 at Hasylab, Hamburg. The crystal temperature was adjusted to 100 K using the liquid-N_2 stream from an Oxford Instruments Cryojet device. A very detailed investigation of scan parameters was undertaken to establish the optimal conditions for data collection with the new Hasylab setup. The details of these investigations are given in the Supporting Information. The best data quality was obtained with a sequence of rather wide 5° ϕ-scans. The upgraded setup at the D3 beamline provided an opportunity to reach very high scattering angles, illustrated here with a maximum $\sin\theta/\lambda$ of 1.56 Å^{-1}. The data set was composed of 180245 reflections, which were integrated and reduced using the XDS program package.[28] The data were averaged to 18698 unique reflections by using the XSCALE module of XDS. Subsequently, 3618 of these intensities were removed based on comparison with model intensities.[13] All discarded reflections had negligible intensity. No absorption correction was applied to the data.

A crucial part of the data reduction was the correction for oblique incidence into the phosphor covering the detector surface. This phosphor was optimized to detect photons at longer wavelengths. However, when working at high-energy synchrotron beamlines the phosphor had partly insufficient absorption and hence it did not detect all scattered photons. If the diffracted beams penetrate the phosphor, the distance within the phosphor, and thus the incident angle, becomes important. In our previous synchrotron charge-density studies, a correction for oblique incidence was a standard[13,29] based on measured transmission factors for the phosphor of a Bruker R6000 CCD detector.[26]

To carry out the same type of correction for the data from beamline D3 at Hasylab, the energy dependence of the transmission factor in a piece of phosphor delivered by Marresearch, matching the thickness and type used in the used Mar165 CCD detector, was measured, Figure 11 (top). A local program was written to perform the correction on XDS output files,[30] and Figure 11 (bottom) shows the effect of the oblique incidence correction on the integrated intensities. The gray points are the ratio of I(corrected) to I(uncorrected) for data collected with the detector at $2\theta=30°$. This value is also indicated by the left vertical black line, which as anticipated coincides with a factor of 1.0. Similarly, the black data points correspond to data collected with the detector at 70°. As can be seen the correction for a large detector such as the MAR165 CCD amounts to up to 20% with 0.55 Å radiation. It is therefore a very important correction and parameters obtained from noncorrected data are inaccurate. Indeed it may be worthwhile to also carry out the correction in protein crystallographic studies based on MarCCD data, although these are typically carried out at longer wave lengths.

100 K single-crystal conventional X-ray data: A colorless crystal with dimensions $0.15\times0.22\times0.25$ mm was fixed with oil to a glass pin sitting on a piece of copper wire. This was attached to a brass pin, arranged on a goniometer head and placed in a Bruker-Nonius Apex2 diffractometer at the University of Aarhus (Denmark). A total of six series of frames were collected at a crystal temperature of 100(2) K generated by an Oxford Cryosystems CryostreamPlus liquid N_2 device. With the program SAINT+,[25] a total of 25061 integrated intensities corrected for Lorentz and polarization effects were obtained. The intensities were corrected for absorption by using the empirical method of SORTAV, giving minimum and maximum transmission coefficients of 0.77 and 0.82, respectively. Scaling and merging using SORTAV[27] resulted in 7212 unique reflections. Of these, 6589 reflections were measured more than once with an overall redundancy of the data set of 3.4. The data set was virtually complete to a resolution of 0.47 Å, although six low-order reflections were missing due to an unfortunate crystal mounting. The maximum $\sin\theta/\lambda$ of the data set is 1.18 Å^{-1}.

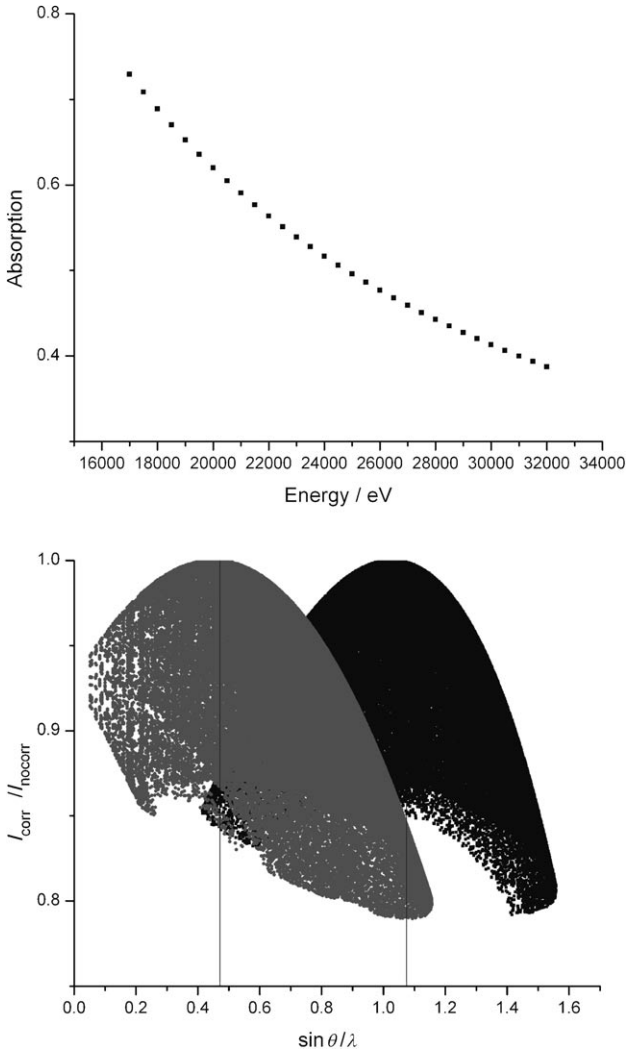

Figure 11. Top: Absorption factor of the Mar165 CCD phosphor as a function of X-ray energy. Bottom: Oblique correction of the Hasylab data. The plot shows I(corrected)/I(uncorrected) for 2θ-value at 30° (gray) and 70° (black).

Charge-density refinement: The procedures used to describe the structural and electronic parameters were identical for all three data sets, apart from some of the modeling of the 16 K APS data, which will be explained in a separate paragraph below. The structure for each data set was independently solved using the direct methods program, SHELXS-97.[31] All non-hydrogen atoms were initially located and subsequently their positions as well as anisotropic atomic displacement parameters (ADPs) were refined using the least-squares refinement program, SHELXL-97.[30]

For refinement of the charge densities, the independent atom model (IAM) of SHELXL was imported into the multipole refinement package XD.[32] This program employs the Hansen–Coppens multipole model to analytically describe the aspherical electron density.[33] To enhance the comparability of the resulting models, a common approach was adopted in which the initial refinement was a high-order refinement of the structural parameters only ($\sin\theta/\lambda>0.8$ Å^{-1}). This was followed by a series of refinements wherein the level of multipoles was increased incrementally such that the final model included all symmetry-allowed multipoles up to hexadecapole level for Mn, and up to octupole level for the remaining

non-hydrogen atoms. For the hydrogen atoms, the distances to their nearest neighbor were fixed according to literature neutron diffraction values, while monopoles and bond-directed dipoles were refined. At this point, the radial κ parameters were refined with the other parameters frozen. It was decided to use separate κ values for the two distinct Mn atoms, as well as one κ for each of the other atom types: O, C, and H (for H, κ was fixed at 1.2). Finally, all parameters were refined freely, which resulted in quick convergence without significantly changing the model. The reliability of the resulting ADPs was checked with the rigid bond test suggested by Hirshfeld,[34] in which the components of the ADPs along the bond direction are compared for bonded atoms. For the models reported here the difference ADPs along bond directions were in all cases less than 10×10^{-4} Å^2.

Results from a single-crystal neutron diffraction study of **1** at 15 K can be found in the literature.[6] An attempt was made to include this information in the refinement of the X-ray structure factors by using a partial X-N procedure, for which only hydrogen parameters were obtained from the neutron data.[35] The X-N refinements were not satisfactory, and the derived CD was inferior to the X-ray only results. As discussed by Iversen et al., the X-N method may suffer from significant differences in systematic errors between the X-ray and neutron data even when each data set is very precise.[35a] In the present case the main problem probably is that the quality of the neutron data is not on a level with the X-ray data. Details about the X-N analysis are given in the Supporting Information.

CCDC 652048–652050 contain the supplementary crystallographic data for this paper. These data can be obtained free of charge from The Cambridge Crystallographic Data Centre via www.ccdc.cam.ac.uk/data_request/cif.

Acknowledgements

Allocation of beamtime at ChemMatCARS at the Advanced Photon Source, Argonne National Laboratory, and at beam line D3 at Hasylab, DESY, is gratefully acknowledged. The work was supported by Dansync. The Carlsberg Foundation is thanked for funding a PPMS system. We thank an anonymous referee for advice on experimental orbital populations.

[1] a) S. Kitagawa, R. Kitaura, S. Noro, *Angew. Chem.* **2004**, *116*, 2388–2430; *Angew. Chem. Int. Ed.* **2004**, *43*, 2334–2375; b) J. Y. Lu, *Coord. Chem. Rev.* **2003**, *246*, 327–347; c) M. Eddaoudi, D. Moler, H. Li, T. M. Reineke, M. O'Keeffe, O. M. Yaghi, *Acc. Chem. Res.* **2001**, *34*, 319–330.

[2] a) M. Eddaoudi, J. Kim, N. Rosi, D. Vodak, J. Wachter, M. O'Keeffe, O. M. Yaghi, *Science* **2002**, *295*, 469–472; b) H. K. Chae, D. Y. Siberio-Pérez, J. Kim, Y. Go, M. Eddaoudi, A. J. Matzger, M. O'Keefe, O. M. Yaghi, *Nature* **2004**, *427*, 523–527; c) N. Rosi, M. Eddaoudi, D. Vodak, J. Eckert, M. O'Keeffe, O. M. Yaghi, *Science* **2003**, *300*, 1127–1129.

[3] a) D. J. Price, S. Tripp, A. K. Powell, P. T. Wood, *Chem. Eur. J.* **2001**, *7*, 200–208; b) E. Tynan, P. Jensen, N. R. Kelly, P. E. Kruger, A. C. Lees, B. Moubaraki, K. S. Murray, *Dalton Trans.* **2004**, 3440–3447; c) V. K. Peterson, Y. Liu, C. M. Brown, C. J. Kepert, *J. Am. Chem. Soc.* **2006**, *128*, 15578; d) J. Halder, C. J. Kepert, B. Moubaraki, K. S. Murray, J. D. Cashion, *Science* **2002**, *298*, 1762; e) A. L. Goodwin, K. W. Chapman, C. J. Kepert, *J. Am. Chem. Soc.* **2005**, *127*, 17980.

[4] a) K. Osaki, Y. Nakai, T. Watanabé, *J. Phys. Soc. Jpn.* **1963**, 18, 919; b) K. Osaki, Y. Nakai, T. Watanabé, *J. Phys. Soc. Jpn.* **1964**, *19*, 717–723.

[5] a) R. B. Filippen, S. A. Friedberg, *J. Chem. Phys.* **1963**, *38*, 2652–2657; b) H. Abe, M. Matsuura, *J. Phys. Soc. Jpn.* **1964**, *19*, 1867–1880; c) R. D. Pierce, S. A. Friedberg, *Phys. Rev.* **1968**, *165*, 680–687; d) H. Abe, H. Morigaki, M. Matsuura, K. Torii, *J. Phys. Soc. Jpn.* **1964**, *19*, 775–775; e) H. Abe, K. Torri, *J. Phys. Soc. Jpn.* **1965**, *20*, 183–184; f) E. F. Bertaut, P. Burlet, P. Burlet, *Solid State Commun.* **1969**, *7*, 343–349; g) M. Matsuura, K. Koyama, Y. Murakami, *J. Phys. Soc. Jpn.* **1985**, *54*, 2714–2719; h) K. Yamagata, *J. Phys. Soc. Jpn.* **1967**, *22*, 582–589; i) K. Yamagata, H. Abe, *J. Phys. Soc. Jpn.* **1965**, *20*, 906–910; j) P. Burlet, P. Burlet, E. F. Bertaut, G. Roult, A. de Combarieu, *Solid State Commun.* **1969**, *7*, 1403–1408.

[6] P. Radhakrishna, B. Gillon, G. Chevrier, *J. Phys. Condens. Matter* **1993**, *5*, 6447–6460.

[7] a) K. Takeda, K. Kawasaki, *J. Phys. Soc. Jpn.* **1971**, *31*, 1026–1036; b) P. Burlet, P. Burlet, J. Rossat-Mignod, A. De Combarieu, E. Bedin, *Phys. Status Solidi B* **1975**, *71*, 675–685; c) H. Kageyama, D. I. Khomskii, R. Z. Levitin, A. N. Vasil'ev, *Phys. Rev. B* **2003**, *67*, 224422; d) R. D. Pierce, S. A. Friedberg, *Phys. Rev. B* **1971**, *3*, 934–942; e) G. R. Hoy, S. De S. Barros, F. De S. Barros, S. A. Friedberg, *J. Appl. Phys.* **1965**, *36*, 936–937.

[8] K. Zenmyo, H. Kubo, M. Tokita, K. Yamagata, *J. Phys. Soc. Jpn.* **2006**, *75*, 104704.

[9] a) R. D. Poulsen, A. Bentien, M. Chevalier, B. B. Iversen, *J. Am. Chem. Soc.* **2005**, *127*, 9156–9166; b) R. D. Poulsen, A. Bentien, T. Graber, B. B. Iversen, *Acta Crystallogr. Sect. A* **2004**, *60*, 382–389.

[10] S. Pillet, M. Souhassou, C. Lecomte, P. Rabu, M. Drillon, C. Massobrio, *Phys. Rev. B* **2006**, *73*, 115116.

[11] N. W. Ashcroft, N. D. Mermin, *Solid State Physics*, CBS Asia, Philidelphia, **1976**.

[12] J. Overgaard, unpublished results based on data collected at the D3 beamline at Hasylab

[13] B. B. Iversen, F. K. Larsen, A. A. Pinkerton, A. Martin, A. Darovsky, P. A. Reynolds, *Acta Crystallogr. Sect. B* **1999**, *55*, 363–374.

[14] R. F. W. Bader, *Atoms in Molecules: A Quantum Theory*, Clarendon, Oxford (UK) **1990**; P. L. A. Popelier, *Atom in Molecules. An Introduction*, Pearson Education, Harlow (UK), **1999**.

[15] A. Volkov, P. Coppens, *Acta Crystallogr. Sect. A*, **2001**, *57*, 395–405.

[16] Yu. A. Abramov, *Acta Crystallogr. Sect. A* **1997**, *53*, 264–272.

[17] a) P. L. A. Popelier, *J. Phys. Chem. A* **1999**, *103*, 2883–2890; b) S. E. O'Brien, P. L. A. Popelier, *J. Chem. Inf. Comput. Sci.* **2001**, *41*, 764–775.

[18] See for example, Figure 24 in B. N. Figgis, B. B. Iversen, F. K. Larsen, P. A. Reynolds, *Acta Crystallogr. Sect. A* **1993**, *49*, 794–806.

[19] Yu. A. Abramov, A. Volkov, P. Coppens, *Chem. Phys. Lett.* **1999**, *311*, 81–86.

[20] a) B. B. Iversen, S. K. Nielsen and F. K. Larsen, *Philos. Mag. A* **1995**, *72*, 1357–1380; b) A. Bentien, E. Nishibori, S. Paschen and B. B. Iversen, *Phys. Rev. B*, **2005**, *71*, 144107.

[21] F. K. Larsen, *Acta Crystallogr. Sect. B* **1995**, *51*, 468–492.

[22] A. Holladay, P. Leung, P. Coppens, *Acta Crystallogr. Sect. A* **1983**, *39*, 377–387.

[23] J. R. Sabino, P. Coppens, *Acta Crystallogr. Sect. A* **2003**, *59*, 127–131.

[24] M. J. Hardie, K. Kirschbaum, A. Martin, A. A. Pinkerton, *J. Appl. Crystallogr.* **1998**, *31*, 815–817.

[25] SAINT, Bruker AXS Inc., Madison, Wisconsin (US), **2005**.

[26] a) G. Wu, B. L. Rodrigues, P. Coppens, *J. Appl. Crystallogr.* **2002**, *35*, 356–359; b) B. B. Iversen, F. K. Larsen, A. Pinkerton, A. Martin, A. Darovsky, P. A. Reynolds, *Inorg. Chem.* **1998**, *37*, 4559–4566.

[27] R. H. Blessing, *J. Appl. Crystallogr.* **1997**, *30*, 421–426.

[28] W. Kabsch, *J. Appl. Crystallogr.* **1993**, *26*, 795–800.

[29] P. Coppens, B. B. Iversen, F. K. Larsen, *Coord. Chem. Rev.* **2004**, *249*, 179–195.

[30] J. Overgaard, G. K. H. Madsen, Program D3_red to reduce data collected at the D3 beamline at Hasylab. Program available from the authors on request.

[31] G. M. Sheldrick, SHELX-97. (Release 97–2), University of Göttingen, Göttingen (Germany), **1997**.

[32] A. Volkov, P. Macchi, L. J. Farrugia, C. Gatti, P. Mallinson, T. Richter, T. Koritsanszky, XD2006 - A Computer Program Package for Multipole Refinement, Topological Analysis of Charge Densities and Evaluation of Intermolecular Energies from Experimental and Theoretical Structure Factors, **2006**.

[33] N. K. Hansen, P. Coppens, *Acta Crystallogr. Sect. A* **1978**, *34*, 909–921.

[34] F. L. Hirshfeld, *Acta Crystallogr. Sect. A* **1976**, *32*, 239–244.

[35] a) B. B. Iversen, F. K. Larsen, B. N. Figgis, P. A. Reynolds and A. J. Schultz, *Acta Crystallogr Sect. B* **1996**, *52*, 923–931; b) B. B. Iversen, F. K. Larsen, P. A. Reynolds and B. N. Figgis, *Acta Chem. Scand.* **1994**, *48*, 800–809; c) B. B. Iversen, F. K. Larsen, B. N. Figgis, P. A. Reynolds, *J. Chem. Soc. Dalton Trans.* **1997**, 13, 2227–2240; d) P. Macchi, B. B. Iversen, A. Sironi, B. C. Chakoumakos, F. K. Larsen, *Angew. Chem.* **2000**, *112*, 2831–2834; *Angew. Chem. Int. Ed.* **2000**, *39*, 2719–2722; e) P. Macchi, F. K. Larsen, A. J. Schultz, B. B. Iversen, *J. Phys. Chem. A* **2001**, *105*, 9231–9242; f) J. Overgaard, B. Schiott, F. K. Larsen, B. B. Iversen, *Chem. Eur. J.* **2001**, *7*, 3756–3767.

Received: May 19, 2007
Published online: November 8, 2007

